PHYSICAL REVIEW B **79**, 184404 (2009)

# Spin dynamics and mode structure in nanomagnet arrays: Effects of size and thickness on linewidth and damping

Justin M. Shaw and T. J. Silva
*Electromagnetics Division, National Institute of Standards and Technology, Boulder, Colorado 80305, USA*

Michael L. Schneider
*Department of Physics and Astronomy, University of Montana, Missoula, Montana 59812, USA*

Robert D. McMichael
*Center for Nanoscale Science and Technology, National Institute of Standards and Technology, Gaithersburg, Maryland 20899, USA*
(Received 29 January 2009; revised manuscript received 7 April 2009; published 5 May 2009)

We use frequency resolved magneto-optic Kerr effect to probe the spin dynamics and mode structure in 50–200-nm-diameter $Ni_{80}Fe_{20}$ nanomagnets ranging from 3 to 10 nm in thickness. We find that the intrinsic Gilbert damping parameter is largely unaffected by the nanopatterning process despite a large linewidth dependence on the size of the nanomagnets. In the larger nanomagnets, both end and center modes are observed. The linewidth of these two modes differ considerably, which is most likely the result of the sensitivity of the end mode to small variations and imperfection of the shape and edge materials. We show that this effect can be exploited as a means to separately characterize the magnetic properties of the nanomagnets as well as the size and shape variations within the array.

DOI: 10.1103/PhysRevB.79.184404 PACS number(s): 75.75.+a, 75.30.Ds, 76.50.+g

## I. INTRODUCTION

Magnetic nanostructures are currently being investigated for magnetic random access memory,[1,2] high-frequency spintronic devices,[3,4] bit patterned media,[5–7] and biological applications.[8] While such technological applications are important in their own right, there is also significant interest to understand how magnetic materials behave when confined to nanoscale dimensions. Questions remain about how to interpret ferromagnetic resonance (FMR) spectra in arrays of nanostructures, how defects affect both the static and high-frequency properties of nanostructures, how to measure and characterize such defects, how micromagnetic simulations or models can be improved to better describe nanostructures, and how lateral confinement affects linewidths and the intrinsic damping parameter. As an example, there are several conflicting reports on the influence of nanofabrication on the intrinsic damping parameter.[9–12] Determination of the damping parameter is critical for the development of high-speed switching technology, high-frequency devices, and theory for spin-momentum transfer. It is also important to understand how scaling and fabrication processes affect switching field distributions, reversal mechanisms, and switching rates.

It was recently shown that the fabrication techniques used to make perpendicularly magnetized nanostructures can significantly alter the anisotropy of the edge region.[5] This edge modification has significant effects on the magnetic reversal properties of the nanostructure that are critical for storage technologies such as bit patterned media and magnetic random access memory. This highlights the fact that magnetic nanostructures cannot be realistically modeled as a homogenous system with uniform magnetic properties throughout. The ability to probe the spin dynamics of nanostructures as well as independently probe the properties at different locations within a nanostructure is thus highly desired.

In addition to modeling the spin dynamics in patterned magnetic structures,[13,14] several experimental techniques have been used in recent years which include ferromagnetic resonance force microscopy,[10,15,16] magneto-optic Kerr effect in the time domain,[17–22] vortex core dynamics,[23–25] Brillouin light scattering (BLS),[26–29] and x-ray microscopy.[30–32] However, the majority of these reports focus on determining the frequency dependencies and/or spatial mode structure, and do not address the measurement of linewidth, and more importantly, separating the intrinsic damping from other contributions to linewidth.

Recently, it was discovered that inhomogeneous dipole fields at the edges of magnetic stripes create localized modes at the edges confined to a few tens of nanometers.[33–36] The behavior of these edge modes differ significantly from the bulk excitations. Extensive work has been carried out on characterizing these edge modes as well as the edge saturation field in magnetic stripes using an inductive FMR technique. It was shown that the edge saturation field, edge mode frequency, and edge mode linewidth depend strongly on the edge roughness and edge tapering.[35,37,38] These results indicate that the edge properties can be separately measured from the bulk magnetic properties via spatially confined modes.

In this report, we present an optical approach to measuring the mode structure in magnetic nanomagnets. By exciting spatially localized modes, we can compare regional properties of the nanostructure without the need of a probe small enough to resolve such features. We will show that the frequency resolved magneto-optic Kerr effect (FR-MOKE) technique we developed has a considerable increase in signal-to-noise ratio (SNR) relative to similar techniques in the time domain which allows for careful evaluation of the mode linewidths. We find significant variation in linewidth

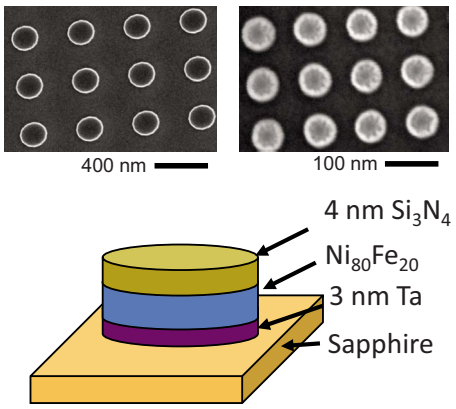


FIG. 1. (Color online) SEM images of (a) nominally 200 nm nanomagnets with 20% ellipticity and (b) nominally 50 nm circular nanomagnets. (c) Schematic diagram of a nanomagnet sample structure.

depending on the mode location and will discuss the implications of the linewidth variation.

## II. EXPERIMENT

Arrays of circular and slightly elliptical nanomagnets were fabricated from dc magnetron sputter-deposited 3 nm Ta, $x$ nm $Ni_{80}Fe_{20}$, and 4 nm $Si_3N_4$ films on sapphire substrates, where $x=3$, 5, and 10 nm. Films were deposited in an applied field to induce an easy anisotropy axis in the film plane. This intrinsic anisotropy field, $\mu_0 H_k$, was measured to be $0.3\pm0.1$, $0.6\pm0.2$, and $0.4\pm0.1$ mT for the 3-, 5-, and 10-nm-thick $Ni_{80}Fe_{20}$ films. Electron beam-lithography was then used to create a cross-linked polymethyl methacrylate (PMMA) mask. The mask pattern was transferred to the deposited magnetic layer with a 300 eV Ar ion mill. The diameters of the nanomagnets were varied from 50 to 200 nm with a pitch (center-to-center spacing) of twice the diameter. Figure 1 shows scanning electron microscope (SEM) images of nominal 50- and 200-nm-diameter nanomagnet arrays as well as a schematic diagram of the idealized nanomagnet structure. The serration along the edges of the 50 nm nanomagnet image is a result of structure on the top surface of the much thicker PMMA masking layer left behind following the ion mill. High-resolution SEM image analysis indicates that the root-mean-square size variation along the short and long axes are typically 2–3 nm.

For simplicity and ease of comparison, we use the *nominal* values of the nanomagnet diameters. This value corresponds to the ideal value of the short axis of the slightly elliptical structure. Unless otherwise stated, the long axis is ideally a 20% larger value resulting in a 20% ellipticity. The *actual* values of the nanomagnet sizes vary slightly from sample to sample and are summarized in Table I as determined from SEM analysis.

The high-frequency mode structure was studied using FR-MOKE. Figure 2 shows a schematic of the FR-MOKE setup. A vector network analyzer (VNA) is used to generate cw microwaves that are amplified to a maximum power of 30 dBm and directed through a coplanar waveguide (CPW) that

TABLE I. Comparison of the nominal diameters and actual size of the nanomagnets for the samples used in this study.

| Nominal diameter | Actual size | | |
|---|---|---|---|
| | 10 nm thickness | 5 nm thickness | 3 nm thickness |
| 200 nm | $235\times215$ nm$^2$ | $220\times202$ nm$^2$ | $228\times205$ nm$^2$ |
| 150 nm | | $165\times151$ nm$^2$ | $168\times154$ nm$^2$ |
| 100 nm | $120\times110$ nm$^2$ | $117\times103$ nm$^2$ | $118\times106$ nm$^2$ |
| 75 nm | | $90\times80$ nm$^2$ | $91\times80$ nm$^2$ |
| 50 nm | $71\times65$ nm$^2$ | $67\times62$ nm$^2$ | $69\times64$ nm$^2$ |

is 50 Ω terminated. The sample is placed on the CPW and aligned with the center conductor that is 150 μm wide; significantly wider than the 20 μm nanomagnet arrays. The thickness of the sapphire substrate is approximately 100 μm, which sets the distance between the nanomagnet arrays and the CPW. We estimate the maximum microwave field in this configuration to be 0.3 mT. An external bias field up to ±500 mT is applied perpendicular to the microwave field direction and parallel to the center conductor. For all measurements in this report, the bias field is directed along the long axis of the elliptical structures, and the rf field is consequently directed along the short axis.

Detection of the magnetodynamic response of the nanomagnets is performed using broadband photodetection of the modulated magneto-optic Kerr effect. Here, a cw low-noise 532 nm diode-pumped solid-state laser is linearly polarized, and focused on the sample at a 45° angle of incidence with a spot size between 10 and 15 μm. The reflected light is collected with a second lens. Because the magneto-optic Kerr effect alters both the polarization angle and ellipticity of the reflected light, we use a compensator to minimize the ellipticity for maximum contrast. The light is analyzed with a polarizer and focused on a broadband 12 GHz free space photoreceiver. The signal from the photodiode is sent to the VNA input port. In this configuration, an $S_{21}$ measurement is performed with the VNA resulting in frequency-swept spec-

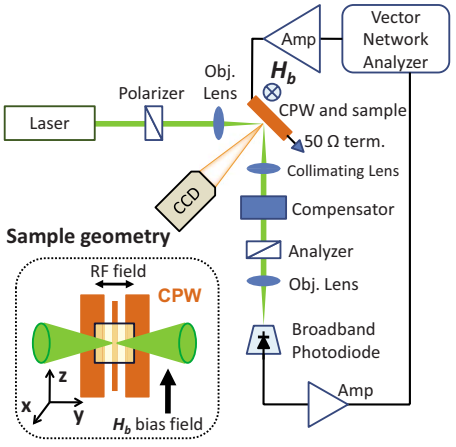


FIG. 2. (Color online) Schematic diagram of the FR-MOKE experimental setup. The inset shows the sample geometry and coordinate system from the perspective of the charge-couple device camera.

tra at a fixed bias field. Although it is reasonable to assume some heating occurs, no effects of laser heating on the frequency or linewidth were observed as verified by attenuation of the incident laser power by two orders of magnitude. This was found not to be the case when glass substrates were used, which have a significantly reduced thermal conductivity compared to sapphire. Similarly, no effects of microwave heating were observed.

The SNR for these measurements was limited by laser noise that was approximately 20 times greater than either shot noise or detector noise at the operational power levels and analyzer settings. The intensity of the light reflected from the sample varied between 10–30 mW and we subsequently adjusted the analyzer such that the light level on the photoreceiver was maintained at 2 mW. Since the relative intensity laser noise is 0.04% in a 200 kHz bandwidth, the resulting relative optical intensity noise of the laser is equivalent to $\approx 2$ nW/Hz$^{1/2}$ at the photoreceiver. The resulting microwave signal immediately after the detector varied from 0.1 to 10 pW, depending on the particular sample and applied field strength, and the microwave noise level were $3\times10^{-18}$ W/Hz. The noise floor of the VNA was $3\times10^{-19}$ W/Hz. Both a transimpedance amplifier with a gain of $R=370\ \Omega$ and a 20 dB microwave low-noise amplifier were used to boost the signal relative to the VNA noise floor.

Spurious background microwave emissions from the coplanar waveguide assembly radiatively coupled to the optical detector, limiting the dynamic range of the measurements. As such, a differential measurement technique was used to subtract the radiatively coupled background from the signal, whereby a spectrum obtained at a large saturating magnetic field of 500 mT was subtracted from the spectrum obtained at the actual measurement field.

To compare properties of the nanomagnets to the intrinsic unpatterned thin film, we fabricated large 20 $\mu$m pad structures alongside the nanomagnet array. We found no measurable difference in the magnetodynamic response of the 20 $\mu$m pad measured in the center and a continuous film of the same thickness, and herein refer to results from the measurement of the 20 $\mu$m pad as the "thin-film" data. An added advantage to using a 20 $\mu$m pad is that it undergoes all the same processing steps as the nanomagnets, and therefore, provides a proper control sample to isolate the effects of confinement in nanomagnets.

It is important to note that this work is focused on measuring the properties of the quasisingle domain state since the high-frequency properties of, for example, the vortex state are quite different.[20,39] We separately measured static hysteresis loops using a focused magneto-optic Kerr effect magnetometer to determine the saturation fields of each array (typically less than 10 mT). In order to ensure the quasisingle domain state, we always saturate the sample at a high field and then decrease the field to the desired value. The data we report here are taken at applied field values above the saturation field precluding the observation of a vortex mode.

Figure 3(a) shows a typical FR-MOKE spectrum and fit where two modes are observed. The FR-MOKE spectra are fit according to the scheme described in Ref. 9 with the addition of including an adjustable phase factor for each mode.

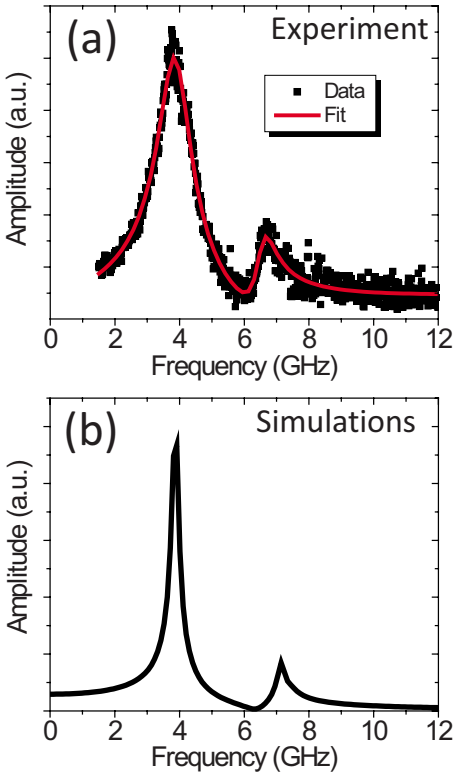


FIG. 3. (Color online) (a) An example of an FR-MOKE spectrum of an array of 100 nm nanomagnets. The fit to the data is included and shows the asymmetry of the peaks due to a nonzero phase relationship between the two resonances. (b) A simulated spectrum of a 100 nm nanomagnet reproducing the asymmetry in the peaks and showing a significantly narrower linewidth for the lower frequency peak.

A significant characteristic of this spectrum is the asymmetry of each of the two peaks and the null between the peaks. The null is a result of interference between the modes. This demonstrates the FR-MOKE technique's sensitivity to the relative phase of modes, in contrast to techniques such as BLS.

OOMMF simulations[40] were used to visualize the excited mode structure in single nanomagnets[41] and to interpret the FR-MOKE data. Magnetostatic edge corrections were used to compensate for the geometrical errors in curved dot boundaries modeled on square computational grids.[42] Figure 3(b) shows an example of a simulated FR-MOKE spectrum. Two features are immediately apparent: (1) the interference null between the two peaks is reproduced in the simulations, and (2) the linewidth of the low-frequency mode in the simulated data is significantly smaller than that of the measured spectrum. The latter point will be addressed at length in Secs. III and IV.

## III. RESULTS

Figure 4(a) shows the contour plot of the frequency spectra for a 10-nm-thick 20 $\mu$m $Ni_{80}Fe_{20}$ square pad that shows the ferromagnetic resonance mode. Figures 4(b)–4(d) show the spectra plots for the 50-, 100-, and 200-nm-diameter nanomagnet arrays, respectively, patterned from the same thin

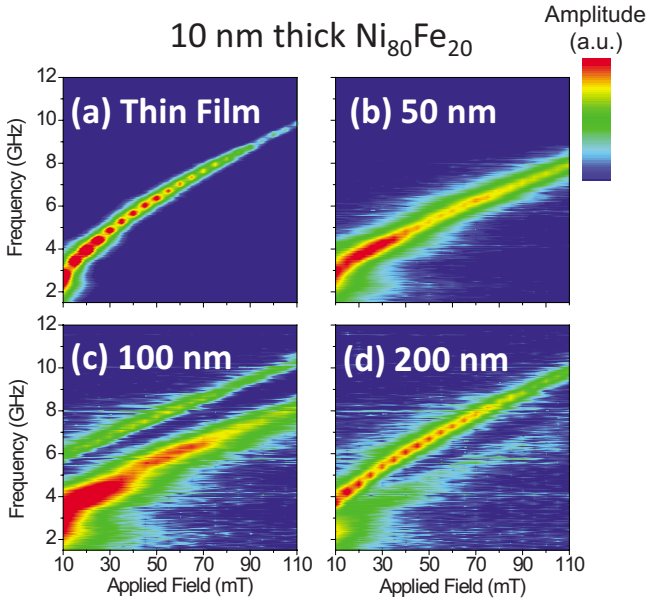


FIG. 4. (Color online) Contour plots of spectra for 10-nm-thick $Ni_{80}Fe_{20}$ for the (a) thin film, (b) 50-nm-diameter, (c) 100-nm-diameter, and (d) 200-nm-diameter nanomagnet arrays. The scale bar represents the normalized amplitude.

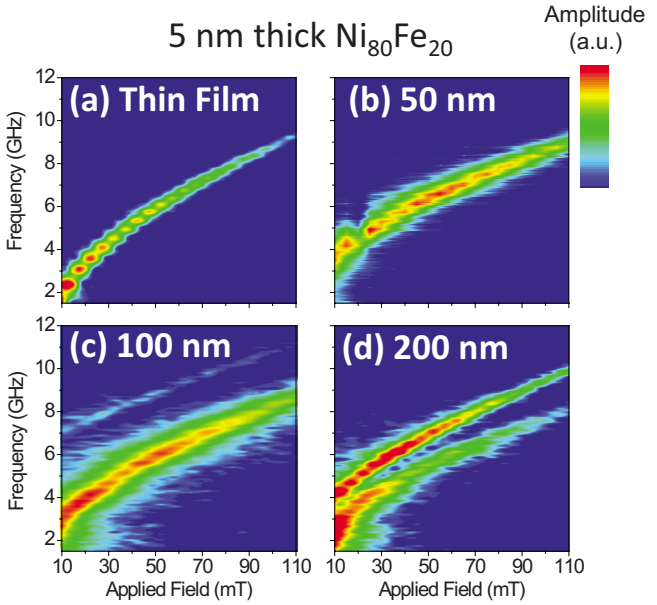


FIG. 5. (Color online) Contour plots of spectra for 5-nm-thick $Ni_{80}Fe_{20}$ for the (a) thin film, (b) 50-nm-diameter, (c) 100-nm-diameter, and (d) 200-nm-diameter nanomagnet arrays. The scale bar represents the normalized amplitude.

film. The two-dimensional contour plots are generated from individual spectra, each acquired at a given applied field. Interpolation of the data was required to form a complete two-dimensional data array for plotting. We caution that some features of the contour plots are artifacts resulting from numerical interpolation. In all cases, the mode amplitude is normalized to the maximum value in a particular data set. (Absolute values of amplitude are difficult to extract with this scheme since it is very dependent on the exact optical alignment and variation in signal due to diffraction of the incident beam with the two-dimensional nanomagnet lattice.[19]) The 50 nm arrays exhibit a broader linewidth than the thin-film resonance that was previously attributed to an increase in the inhomogenous component of the linewidth due to nonuniformity of the nanomagnet size across the array.[9] In the 100 and 200 nm cases, two modes are observed, with the higher frequency mode increasing in relative amplitude as the diameter is increased.

As the thickness of $Ni_{80}Fe_{20}$ is decreased to 5 nm (Fig. 5), the same trend in mode amplitudes is observed except that the higher frequency mode is barely detectable at a 100 nm diameter. This suggests that this mode becomes further suppressed as the thickness is decreased. Indeed, as the $Ni_{80}Fe_{20}$ thickness is further reduced to 3 nm (Fig. 6), the higher frequency mode is not evident until the diameter is increased to 150 nm (not shown).

The resonance frequency $f_0$ and frequency-swept linewidth $\Delta f$ of the modes are determined by the fitting routine described in Ref. 9 for each constant field spectrum. The field dependence of $f_0$ is described by the Kittel equation as follows:

$$f_0 = \left(\frac{\gamma\mu_0}{2\pi}\right)\sqrt{(H_b + H_k + H_1)(H_b + H_k + H_2)}, \qquad (1)$$

where

$$H_1 = (N_y - N_z)M_s, \qquad (2)$$

$$H_2 = (N_x - N_z)M_s, \qquad (3)$$

and $\gamma = (g\mu_B)/\hbar$ is the gyromagnetic ratio, $g = 2.07$ is the spectroscopic splitting factor, $\mu_B$ is the Bohr magneton, $\hbar$ is Planck's constant, $\mu_0$ is the permeability of free space, $H_b$ is the applied bias field, $H_k$ is the intrinsic anisotropy field,

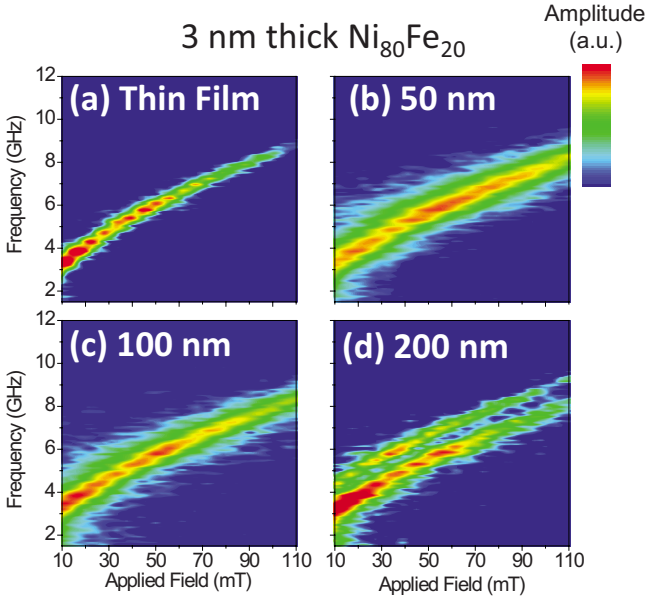


FIG. 6. (Color online) Contour plots of spectra for 3-nm-thick $Ni_{80}Fe_{20}$ for the (a) thin film, (b) 50-nm-diameter, (c) 100-nm-diameter, and (d) 200-nm-diameter nanomagnet arrays. The scale bar represents the normalized amplitude.

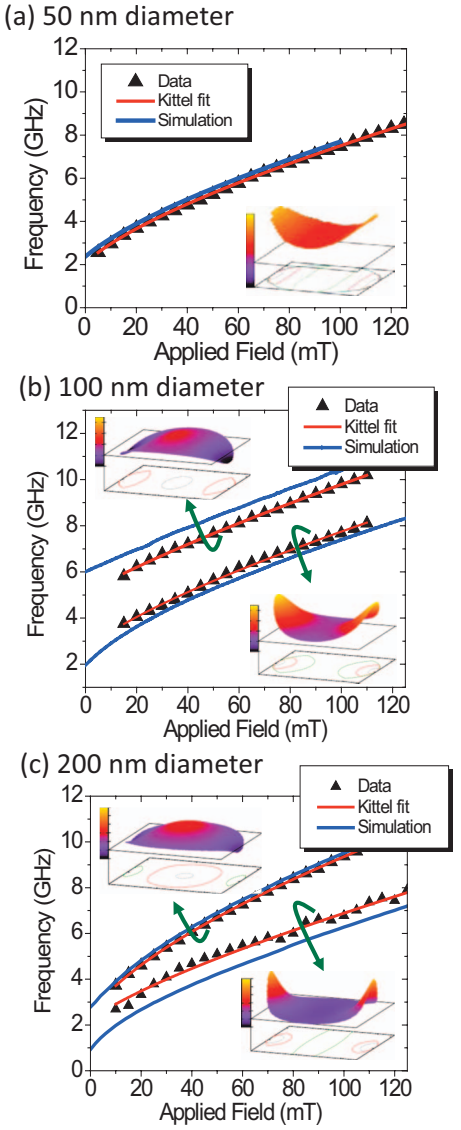


FIG. 7. (Color) Plots of $f_0$ vs $H_b$ for 10-nm-thick $Ni_{80}Fe_{20}$ for (a) 50-, (b) 100-, and (c) 200-nm-diameter nanomagnet arrays. Fits of Eq. (1) to the experimental data (▲) are included as the red solid line. Simulations performed for single nanomagnets of the same size (blue line) show reasonable agreement with the experimental data. The insets in each figure show the relative amplitude of precession across the nanomagnet for each mode obtained from the simulations. The horizontal plane in the insets indicates where the amplitude is zero.

$N_{x,y,z}$ are the effective demagnetizing factors, and $M_s$ is the saturation magnetization. Figure 7 shows some examples of the Kittel equation fits to frequency versus applied bias field data. The values of $H_1$ and $H_2$ for each mode are determined from these fits.

We performed micromagnetic simulations in order to understand the mode structure and trends observed in Figs. 4–6. Figure 7(a) shows data for $f_0$ vs $H_b$, the associated fits to the Kittel equation, and the simulation results for a 50-nm-diameter 10-nm-thick sample. Both the experiment and simulation reveal only a single mode with significant amplitude within this frequency range. The inset shows a three-dimensional plot of the relative precession amplitude across the nanomagnet structure from the simulations. The mode excited in this small structure has a relatively large amplitude throughout the entire structure with larger precession at the ends.

The simulations also reproduce the presence of two modes in the 100- and 200-nm-diameter structures. The simulated frequencies are plotted with the experimental data in Figs. 7(b) and 7(c), respectively. The field dependence of the simulated data (blue line) agrees reasonably well with the experimental data. We speculate that the small frequency shifts between the simulations and the data is a result of the fact that the simulations are performed on ideal structures, which do not take into account such things as sidewall tapering, edge roughness, lithographic defects, and nanomagnet interactions. In contrast to the 50-nm-diameter sample, the two modes are more spatially localized within the nanomagnet structure: the higher frequency mode has a large amplitude concentrated in the center of the nanomagnet, whereas the lower frequency mode is concentrated at the end. As such, we hereafter refer to the higher and lower frequency modes as the "center" and "end" modes, respectively.

The localized mode structure explains the shift in amplitude of the end mode relative to the center mode as the nanomagnet diameter increases, as shown in Fig. 4. At the smallest diameters (<75 nm), the only observed mode is concentrated at the ends although a significant amplitude is also present throughout the entire structure. The modeling also reveals a low-intensity center mode at higher frequencies outside the experimentally accessible range (not shown). As the diameter increases, the low-frequency end mode becomes increasingly localized at the ends. Simultaneously, the center mode emerges as its frequency drops and amplitude increases. As the diameter is increased further, the ratio of the volume occupied by the end mode to that of the center mode decreases. Correspondingly, the relative amplitude of the end mode also decreases with increasing diameter. An interesting result is the fact that the shift of amplitude from the end mode to the center mode occurs at different values of diameter depending on the thickness of the $Ni_{80}Fe_{20}$. We verified that this trend is not simply a result of differences in the susceptibility tensor when using the experimental values of $H_1$ and $H_2$ that were extracted for each mode. However, micromagnetic simulations show the same trend in amplitude observed experimentally and also reveal that the confinement of the end mode decreases as the thickness is reduced.

The spatial localization of the end and center modes permits some capability to independently probe the magnetic properties at the end and interior regions of magnetic nanostructures. We can begin by analyzing the measured linewidths of the modes. Since the FR-MOKE technique measures the *frequency*-swept linewidth ($\Delta f$) directly, we convert this to the *field*-swept linewidth ($\Delta H$) by the following relation:

$$\Delta H = \frac{\Delta f}{\left(\frac{\partial f_0}{\partial H_b}\right)}. \tag{4}$$

Here, the $(\partial f_0/\partial H_b)$ term is taken as the slope in the Kittel equation fits at the particular $f_0$. Figure 8 shows the mea-

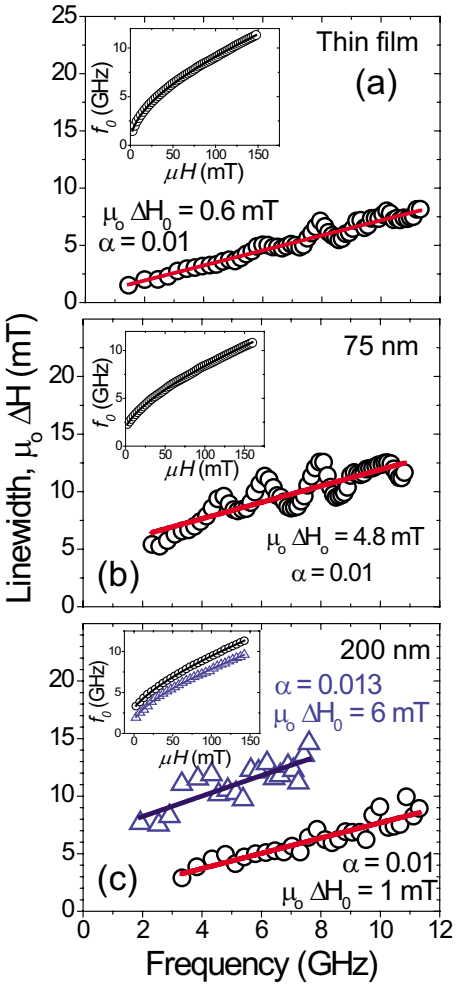


FIG. 8. (Color online) $\Delta H_0$ vs $f_0$ for the 5-nm-thick $Ni_{80}Fe_{20}$ with (a) the thin film, (b) 75-nm-diameter, and (c) 200-nm-diameter arrays. Both the end (△) and center (○) modes are observed in the 200-nm-diameter sample. Fits to Eq. (5) are included that were used to separate the contribution of $\alpha$ and $\Delta H_0$ to the total mode linewidth. The insets show the respective Kittel plots used to convert from $\Delta f$ to $\Delta H$.

sured $\Delta H$ as a function of frequency for the 5-nm-thick samples. In general, the inhomogeneous broadening $\Delta H_0$ is separated from the intrinsic damping $\alpha$ by a linear fit of the following form:

$$\Delta H(f) = \Delta H_0 + \frac{4\pi\alpha}{\gamma\mu_0} f. \tag{5}$$

For the 5 nm thin-film linewidth data presented in Fig. 8(a), a fit to Eq. (5) yields values of $\alpha = 0.01 \pm 0.001$ and $\mu_0 \Delta H_0 = 0.6$ mT, which agrees with previously reported values in unpatterned $Ni_{80}Fe_{20}$ films.[43] For the 75-nm-diameter data shown in Fig. 8(b), there is a significant increase in linewidth due to increased inhomogeneous broadening (4.8 mT ± 0.5 mT) but the Gilbert damping remains constant at $\alpha = 0.01 \pm 0.002$. In the case of the 200 nm sample, where the relative amplitude of both the center and end modes are similar, the linewidths can be independently measured and exhibit a very different behavior. Upon fitting to

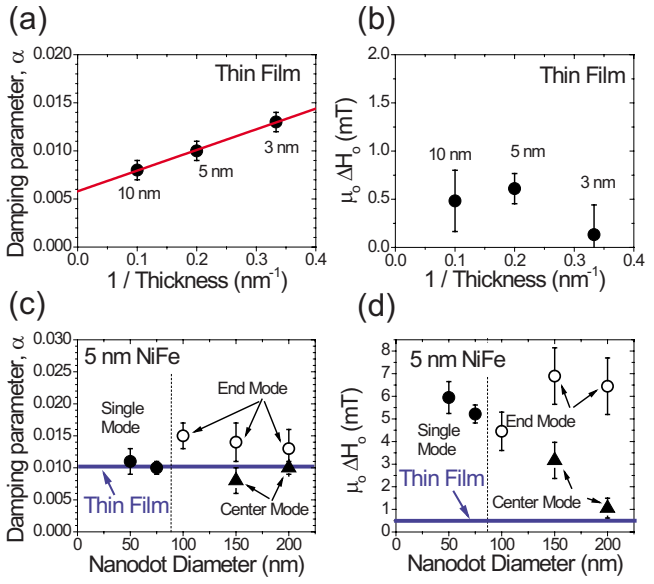


FIG. 9. (Color online) Values of (a) $\alpha$ and (b) $\Delta H_0$ as a function of thin-film thickness, and the diameter dependence of (c) $\alpha$ and (d) $\Delta H_0$ for the 5-nm-thick patterned samples. The vertical dashed line indicates the boundary between regions where single and multiple modes are observed.

Eq. (5) the higher frequency center mode yields a value of $\alpha = 0.01 \pm 0.001$ and $\mu_0 \Delta H_0 = 1.1 \pm 0.5$ mT that approaches the values measured for the thin film. The end mode, however, has a considerable increase in the linewidth, and a fit to Eq. (5) yields values of $\alpha = 0.013 \pm 0.003$ and $\mu_0 \Delta H_0 = 6.4 \pm 1.0$ mT.

The data suggest that the large increase in linewidth is primarily due to increased inhomogeneity. This is supported by micromagnetic simulations on single nanomagnets which produce nearly identical values of linewidth for center and end modes when inhomogeneity is neglected. The increased contribution of inhomogeneity to linewidth for the end mode is not surprising, considering that we are measuring a large number of nanomagnets, and the edge region is defined by a lithographic process and ion mill, both of which can lead to variations between individual nanomagnets. In contrast, the interior region is defined by a much more controlled thin-film deposition process, and thus, should approach that of the thin film.

Because of the increased scatter in the end mode data, there is significant increase in uncertainty in $\alpha$ and $\Delta H_0$. This increased scatter in Fig. 8(c) is a result of the fact that the two modes overlap significantly and the SNR in the end mode is significantly lower than that of the center mode causing increased uncertainty in the end mode fitting. Another source of scatter originates from the "wiggles" present in all the linewidth plots. These features are reproducible in all data sets and are most likely caused by resonances in the CPWs.

The linewidth data for the samples used in this study are summarized in Fig. 9. We first consider the thin-film data in Figs. 9(a) and 9(b). The damping coefficient is seen to increase from 0.008 to 0.013 as the thickness is decreased from 10 to 3 nm, consistent with other previously reported values

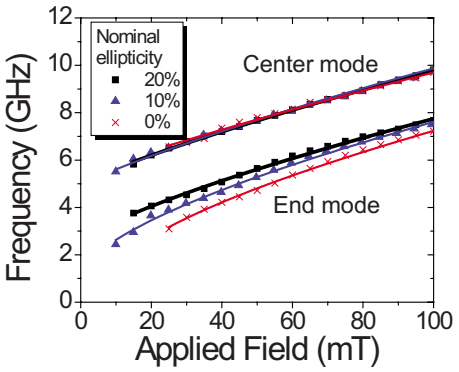


FIG. 10. (Color online) Plots of $f_0$ vs $H_b$ for a 110-nm-diameter nanomagnet array showing the frequency shift in the modes as the nominal ellipticity of the nanomagnets are varied between 0% and 20%.

over this thickness range.[43,44] This variation is most likely the result of spin-pumping effects from the NiFe/Ta interface.[45–47] A linear fit of the $\alpha$ versus the inverse thickness yields an intrinsic value of $\alpha=0.006\pm0.001$. The thickness dependence of the inhomogeneous broadening is constant within error and has a mean value of 0.5 mT indicative of highly homogeneous $Ni_{80}Fe_{20}$ films.

Both $\alpha$ and $\Delta H_0$ are plotted as a function of nanomagnet diameter for the 5-nm-thick case in Figs. 9(c) and 9(d), respectively. The data for the other values of thickness (not shown) produce similar results. We clearly see in Fig. 9(c) that the damping parameter does not vary significantly with nanomagnet size and are within error of the thin-film value of $\alpha=0.01$. This is in contrast with an earlier report which shows a strong size dependence in the damping parameter in Ni nanostructures.[18] However, in that work, the contribution of the intrinsic damping and inhomogeneous term was not separated which could explain the variation they observed. $\Delta H_0$ in Fig. 9(d) is relatively large at the smallest diameters where only a single mode is observed. When both the center and end modes are excited, $\Delta H_0$ for the center mode approaches the thin-film value with increasing diameter while $\Delta H_0$ for the end mode remains large.

## IV. DISCUSSION

The observed inhomogeneous contribution to the end mode linewidth broadening can come from two sources: (1) linewidth broadening due to modification of magnetic properties at the edge, edge roughness, and any other edge-related imperfection, and (2) dot-to-dot variations in size and shape which yield an increased linewidth due to a sum of a distribution of end mode frequencies. Correlation of the end mode linewidth broadening with edge imperfection was observed in magnetic stripes.[38] In the next subsections, we consider how size and shape variations from dot-to-dot affect the linewidth.

### A. Size variation effect on the measured linewidth

We previously accounted for the linewidth broadening in $71\times65$ nm$^2$ structures by variations in nanomagnet size.[9] In this case only a single mode was observed. We found that an uncorrelated dot-to-dot variation of 1 nm in the two in-plane dimensions was sufficient to explain the linewidth broadening measured in the array. This variation was consistent with that measured with SEM image analysis as well as the switching field distributions obtained from the hysteresis curves of the arrays.

TABLE II. Stiffness field sensitivities to dimensional variations for a $220\times202$ nm$^2$ nanomagnet with 5-nm-thick $Ni_{80}Fe_{20}$.

| | End mode (mT/nm) | Center mode (mT/nm) |
|---|---|---|
| $\mu_0(\partial H_1/\partial z)$ | $0.16\pm0.01$ | $-0.011\pm0.01$ |
| $\mu_0(\partial H_2/\partial z)$ | $0.21\pm0.03$ | $0.54\pm0.04$ |
| $\mu_0(\partial H_1/\partial y)$ | $-0.205\pm0.005$ | $-0.193\pm0.002$ |
| $\mu_0(\partial H_2/\partial y)$ | $-1.36\pm0.04$ | $0.10\pm0.01$ |

We experimentally observe such an effect on mode linewidth by measuring a set of arrays where the ellipticity is varied. Figure 10 shows the frequency versus applied field for an additional sample where the short axis is held constant at 110 nm, and the long axis is varied from 110 to 132 nm (corresponding to a 0–20% variation in ellipticity in the structures). The higher frequency center mode shows a negligible frequency shift with varying ellipticity. However, the end mode exhibits significant frequency shift as a function of ellipticity. (The frequency shift is as much as 1 GHz at low fields.) This is consistent with the end mode being much more sensitive to shape than the center mode.

The question remains as to whether such size variations can account for the two different linewidth trends observed in Fig. 8(c). We apply the same method used in Ref. 9 to both modes in the $220\times202$ nm$^2$ nanostructure array. Micromagnetic simulations were performed on structure where the dimensions were varied in each direction. The stiffness field sensitivities for each mode were then determined through fits of Eq. (1) to the data obtained while one dimension was varied. The resulting stiffness field sensitivities are given in Table II.

Using a first-order approximation, the standard deviation of the resonant field distribution is given in Eq. (6),

$$\sigma_H = \frac{H_b + H_2}{2H_b + H_1 + H_2}\delta H_1 + \frac{H_b + H_1}{2H_b + H_1 + H_2}\delta H_2, \qquad (6)$$

where

$$\delta H_i = \sqrt{\left(\frac{\partial H_i}{\partial z}\delta z\right)^2 + \left(\frac{\partial H_i}{\partial y}\delta y\right)^2}. \qquad (7)$$

Here, $H_i$ is either $H_1$ or $H_2$, and $\delta z$ and $\delta y$ are the standard deviations of the nanomagnet dimensions along the $z$ and $y$ axes, respectively. We assume that the size variations are uncorrelated between the two axes. For a Gaussian distribution, the inhomogeneous broadening contribution due to size variations is then:

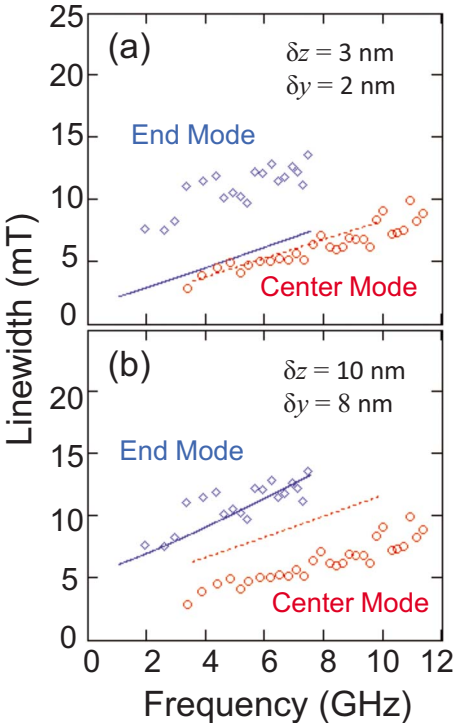


FIG. 11. (Color online) Plot of $\Delta H_0$ vs $f_0$ 5-nm-thick $220\times202$ nm$^2$ nanomagnet array along with data taken from the size distribution model with (a) the size fluctuation measured in SEM analysis, and (b) a best fit of the size fluctuations to the end mode data.

$$\Delta H_0' = 2(2\ \ln\ 2)^{1/2}\sigma_H = (2.355)\sigma_H. \tag{8}$$

SEM image analysis of this array yields values of $\delta z=3$ nm and $\delta y=2$ nm. By combining Eq. (8) for the inhomogenous broadening term and Eq. (5), we can plot the expected linewidth for such dimensional fluctuations. These are given in Fig. 11(a) with the experimental data. It is clear that the end mode has an increased linewidth relative to the center mode but, for these dimensional fluctuations, it is not enough to explain the severity of the increase that we observe. In order to fit the linewidth data for the end mode, values of $\delta z=10$ nm and $\delta y=8$ nm were necessary. However, these values are not consistent with SEM images and, as Fig. 11(b) shows, the linewidth data for the center mode cannot be simultaneously fit using such large values for $\delta z$ and $\delta y$. These results show that variations in size cannot fully explain the linewidth broadening observed for the end modes.

We note that the slope of the linewidth data is also affected by the size distributions. This is most pronounced in the end mode linewidth as observed in Fig. 11. The effect originates from the fact that $\sigma_H$ in Eq. (6) is a function of the applied bias field. This change in slope can influence the measured value of $\alpha$ through a fit to Eq. (5) and may explain the slightly higher values of $\alpha$ measured for the end mode relative to the thin film [Fig. 9(c)] although enhanced damping at the edge cannot be completely ruled out.

### B. Shape variation effects on linewidth

In addition to size variations, we simulate the effect of shape variation from the ideal elliptical shape of the nanomagnets. We define the shape of a distorted ellipse with an egglike shape with the following relation:

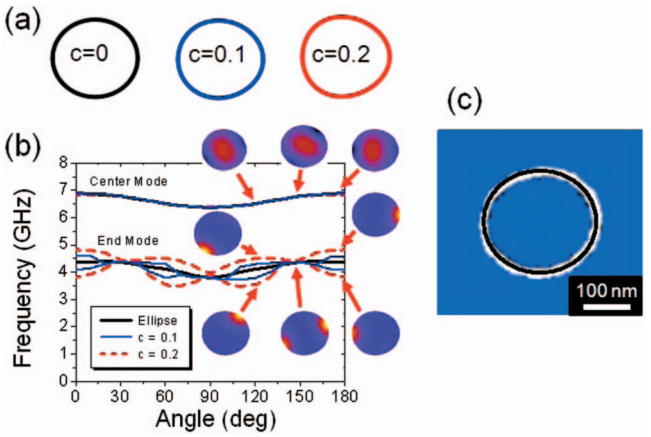


FIG. 12. (Color) (a) Images of the nanomagnet shape used to simulate the effect of egglike shape distortion obtained for values of $c=0$, 0.1, and 0.2. (b) The simulated frequency versus applied field angle for these three nanomagnet shapes. The insets show the amplitude of precession across the nanomagnet structure for each mode where yellow is the highest amplitude and dark blue represents zero amplitude. (c) SEM image of a $220\times202$ nm$^2$ nanomagnet that has been enhanced to show the edge boundary. An ellipse is overlaid to show the deviation of the sample from the nominal shape.

$$\frac{z^2}{A} + \frac{y^2}{Be^{-cz}} = 1, \tag{9}$$

where $A$ and $B$ are constants that define the elliptical shape, and $c$ is a constant that defines the amount of egglike distortion. Examples of the resulting shapes for $c=0$, 0.1, and 0.2 for a $235\times215$ nm$^2$ ($c=0$) structure are given in Fig. 12(a). Micromagnetic simulations were also performed on these three shapes. The calculated mode frequencies as a function of in-plane applied field angle with magnitude 50 mT is given in Fig. 12(b). As observed with the size variations, the center mode also shows very little change in frequency with the distortion. However, the end mode shows large shifts in frequency, and at certain angles, splits into two frequencies. It is seen that the two end modes have nondegenerate frequencies over a wide range of applied field angles. The frequencies seem to be largely influenced by the curvature of the nanomagnet outline wherever the end mode is localized [insets of Fig. 12(b)]. Sharper curvatures are seen to produce higher end mode frequencies.

Although extremely difficult to quantify, variations in shape and curvature from dot-to-dot are to be expected in large ensembles of lithographically defined nanostructures. Figure 12(c) shows an enhanced SEM image of a nanomagnet with an overlaid perfect ellipse. While the nanomagnet is seen to be close to a perfect ellipse, there is a slight distortion. The location and nature of this distortion varies from dot to dot.

These simulations suggest that the curvature of the end region has a larger influence on the end mode frequency than the size itself, and could explain why size variations alone

are not sufficient to explain our experimental data. From an applied technology standpoint, this suggests that, if such a center mode can be exploited for reversal or high-frequency applications, effects due to device-to-device variation stemming from lithographic variations or nonideal shape will be minimized.

Finally, the picture is further complicated by considering interactions among nanomagnets in a periodic array. Although beyond the scope of the present work, our initial calculations of the influence of such interactions indicate that dipole field interactions can have a narrowing effect on the ensemble linewidth at lower frequencies. As a result, the amount of dot-to-dot variation required may be even greater than that extracted from the measured linewidths via the method described here. With the present setup, we are unable to separate the components of $\Delta H_0$ originating from intrinsic edge properties of the nanomagnets to those created by dot-to-dot variations (with due consideration of interaction effects). Such separation will require comparison of mode linewidths in individual nanostructures to identical nanostructures in large arrays. For example, an increase in end mode linewidth in an individual nanomagnet would indicate an intrinsic source of broadening such as edge roughness or oxidation. Comparison of such measured linewidths in individual nanomagnets to those measured in arrays with differing pitch can be used to determine the additional broadening caused by dot-to-dot variations and isolate effects of interactions (i.e., interaction strength will vary with the array pitch). While such measurements are beyond the scope of the present work, this report demonstrates that analysis of the measured mode structure allows for the separate determination of localized high-frequency properties at the edge and interior regions, and that those properties can have significant differences.

## V. SUMMARY

We have measured the spin dynamics in 50–200 nm $Ni_{80}Fe_{20}$ nanostructures using the FR-MOKE technique. The mode structure of these nanostructures was confirmed by micromagnetic simulations, and shows that, above a critical size, both center and end modes are observed. The increased SNR of FR-MOKE allows us to carefully evaluate the linewidth of these excited modes which allows us to directly measure the damping parameter and inhomogeneous broadening term for each mode. The significant difference in linewidth between the two modes is most likely a result of the end mode being highly sensitive to imperfections, size distributions, and variations in shape as opposed to a change in intrinsic damping.

## ACKNOWLEDGMENTS

The authors are grateful to Hans Nembach and Pavel Kabos for valuable discussions, and Roy Geiss for SEM imaging support.

[1] B. N. Engel, J. Akerman, B. Butcher, R. W. Dave, M. DeHerrera, M. Durlam, G. Grynkewich, J. Janesky, S. V. Pietambaram, N. D. Rizzo, J. M. Slaughter, K. Smith, J. J. Sun, and S. Tehrani, IEEE Trans. Magn. **41**, 132 (2005).

[2] S. Kaka, M. R. Pufall, W. H. Rippard, T. J. Silva, S. E. Russek, J. A. Katine, and M. Carey, J. Magn. Magn. Mater. **286**, 375 (2005).

[3] S. I. Kiselev, J. C. Sankey, I. N. Krlvorotov, N. C. Emley, R. J. Schoelkopf, R. A. Buhnnan, and D. C. Ralph, Nature (London) **425**, 380 (2003).

[4] A. M. Deac, A. Fukushima, H. Kubota, H. Maehara, Y. Suzuki, S. Yuasa, Y. Nagamine, K. Tsunekawa, D. D. Djayaprawira, and N. Watanabe, Nat. Phys. **4**, 803 (2008).

[5] J. M. Shaw, S. E. Russek, T. Thomson, M. J. Donahue, B. D. Terris, O. Hellwig, E. Dobisz, and M. L. Schneider, Phys. Rev. B **78**, 024414 (2008).

[6] T. Thomson, G. Hu, and B. D. Terris, Phys. Rev. Lett. **96**, 257204 (2006).

[7] B. D. Terris and T. Thomson, J. Phys. D **38**, R199 (2005).

[8] G. Zabow, S. Dodd, J. Moreland, and A. Koretsky, Nature (London) **453**, 1058 (2008).

[9] M. L. Schneider, J. M. Shaw, A. B. Kos, T. Gerrits, T. J. Silva, and R. D. McMichael, J. Appl. Phys. **102**, 103909 (2007).

[10] O. Klein, G. de Loubens, V. V. Naletov, F. Boust, T. Guillet, H. Hurdequint, A. Leksikov, A. N. Slavin, V. S. Tiberkevich, and N. Vukadinovic, Phys. Rev. B **78**, 144410 (2008).

[11] J. C. Sankey, P. M. Braganca, A. G. F. Garcia, I. N. Krivorotov, R. A. Buhrman, and D. C. Ralph, Phys. Rev. Lett. **96**, 227601 (2006).

[12] N. C. Emley, I. N. Krivorotov, O. Ozatay, A. G. F. Garcia, J. C. Sankey, D. C. Ralph, and R. A. Buhrman, Phys. Rev. Lett. **96**, 247204 (2006).

[13] M. Grimsditch, L. Giovannini, F. Montoncello, F. Nizzoli, G. K. Leaf, and H. G. Kaper, Phys. Rev. B **70**, 054409 (2004).

[14] M. Grimsditch, G. K. Leaf, H. G. Kaper, D. A. Karpeev, and R. E. Camley, Phys. Rev. B **69**, 174428 (2004).

[15] T. Mewes, J. Kim, D. V. Pelekhov, G. N. Kakazei, P. E. Wigen, S. Batra, and P. C. Hammel, Phys. Rev. B **74**, 144424 (2006).

[16] Y. Obukhov, D. V. Pelekhov, J. Kim, P. Banerjee, I. Martin, E. Nazaretski, R. Movshovich, S. An, T. J. Gramila, S. Batra, and P. C. Hammel, Phys. Rev. Lett. **100**, 197601 (2008).

[17] A. Barman, S. Q. Wang, J. D. Maas, A. R. Hawkins, S. Kwon, A. Liddle, J. Bokor, and H. Schmidt, Nano Lett. **6**, 2939 (2006).

[18] A. Barman, S. Wang, J. Maas, A. R. Hawkins, S. Kwon, J. Bokor, A. Liddle, and H. Schmidt, Appl. Phys. Lett. **90**, 202504 (2007).

[19] M. Grimsditch, F. Y. Fradin, Y. Ji, A. Hoffmann, R. E. Camley, V. Metlushko, and V. Novosad, Phys. Rev. Lett. **96**, 047401 (2006).

[20] Z. G. Liu, R. D. Sydora, and M. R. Freeman, Phys. Rev. B **77**, 174410 (2008).

[21] D. Wang, A. Verevkin, R. Sobolewski, R. Adam, A. van der Hart, and R. Franchy, IEEE Trans. Nanotechnol. **4**, 460 (2005).

[22] I. Neudecker, K. Perzlmaier, F. Hoffmann, G. Woltersdorf, M.

Buess, D. Weiss, and C. H. Back, Phys. Rev. B **73**, 134426 (2006).
[23] R. L. Compton and P. A. Crowell, Phys. Rev. Lett. **97**, 137202 (2006).
[24] K. S. Buchanan, M. Grimsditch, F. Y. Fradin, S. D. Bader, and V. Novosad, Phys. Rev. Lett. **99**, 267201 (2007).
[25] K. S. Buchanan, P. E. Roy, F. Y. Fradin, K. Yu. Guslienko, M. Grimsditch, S. D. Bader, and V. Novosad, J. Appl. Phys. **99**, 08C707 (2006).
[26] G. Gubbiotti, M. Madami, S. Tacchi, G. Carlotti, A. O. Adeyeye, S. Goolaup, N. Singh, and A. N. Slavin, J. Magn. Magn. Mater. **316**, E338 (2007).
[27] C. Bayer, J. Jorzick, B. Hillebrands, S. O. Demokritov, R. Kouba, R. Bozinoski, A. N. Slavin, K. Y. Guslienko, D. V. Berkov, N. L. Gorn, and M. P. Kostylev, Phys. Rev. B **72**, 064427 (2005).
[28] H. Schultheiss, S. Schafer, P. Candeloro, B. Leven, B. Hillebrands, and A. N. Slavin, Phys. Rev. Lett. **100**, 047204 (2008).
[29] L. Giovannini, F. Montoncello, F. Nizzoli, G. Gubbiotti, G. Carlotti, T. Okuno, T. Shinjo, and M. Grimsditch, Phys. Rev. B **70**, 172404 (2004).
[30] M. T. Bryan, P. W. Fry, P. J. Fischer, and D. A. Allwood, J. Appl. Phys. **103**, 07D909 (2008).
[31] Y. Acremann, J. P. Strachan, V. Chembrolu, S. D. Andrews, T. Tyliszczak, J. A. Katine, M. J. Carey, B. M. Clemens, H. C. Siegmann, and J. Stohr, Phys. Rev. Lett. **96**, 217202 (2006).
[32] J. P. Strachan, V. Chembrolu, Y. Acremann, X. W. Yu, A. A. Tulapurkar, T. Tyliszczak, J. A. Katine, M. J. Carey, M. R. Scheinfein, H. C. Siegmann, and J. Stohr, Phys. Rev. Lett. **100**, 247201 (2008).
[33] J. P. Park, P. Eames, D. M. Engebretson, J. Berezovsky, and P. A. Crowell, Phys. Rev. Lett. **89**, 277201 (2002).
[34] J. Jorzick, S. O. Demokritov, B. Hillebrands, M. Bailleul, C. Fermon, K. Y. Guslienko, A. N. Slavin, D. V. Berkov, and N. L. Gorn, Phys. Rev. Lett. **88**, 047204 (2002).
[35] R. D. McMichael and B. B. Maranville, Phys. Rev. B **74**, 024424 (2006).
[36] O. Gerardin, H. Le Gall, M. J. Donahue, and N. Vukadinovic, J. Appl. Phys. **89**, 7012 (2001).
[37] B. B. Maranville, R. D. McMichael, S. A. Kim, W. L. Johnson, C. A. Ross, and J. Y. Cheng, J. Appl. Phys. **99**, 08C703 (2006).
[38] R. D. McMichael, C. A. Ross, and V. P. Chuang, J. Appl. Phys. **103**, 07C505 (2008).
[39] M. J. Pechan, C. Yu, D. Owen, J. Katine, L. Folks, and M. Carey, J. Appl. Phys. **99**, 08C702 (2006).
[40] M. J. Donahue and D. G. Porter, National Institute of Standards and Technology Interagency Report No. NISTIR 6376, 1999.
[41] R. D. McMichael and M. D. Stiles, J. Appl. Phys. **97**, 10J901 (2005).
[42] M. J. Donahue and R. D. McMichael, IEEE Trans. Magn. **43**, 2878 (2007).
[43] J. P. Nibarger, R. Lopusnik, Z. Celinski, and T. J. Silva, Appl. Phys. Lett. **83**, 93 (2003).
[44] J. O. Rantschler, B. B. Maranville, J. J. Mallett, P. J. Chen, R. D. McMichael, and W. F. Egelhoff, IEEE Trans. Magn. **41**, 3523 (2005).
[45] M. Zwierzycki, Y. Tserkovnyak, P. J. Kelly, A. Brataas, and G. E. W. Bauer, Phys. Rev. B **71**, 064420 (2005).
[46] T. Gerrits, M. L. Schneider, and T. J. Silva, J. Appl. Phys. **99**, 023901 (2006).
[47] G. Woltersdorf, M. Buess, B. Heinrich, and C. H. Back, Phys. Rev. Lett. **95**, 037401 (2005).